

Chemical Evolution of HC_3N in Dense Molecular Clouds

Naiping Yu^{1,2*}, Jun-Jie Wang^{1,2}, Jin-Long Xu¹

¹National Astronomical Observatories, Chinese Academy of Sciences, Beijing 100012, China

²NAOC-TU Joint Center for Astrophysics, Lhasa 850000, China

17 October 2019

ABSTRACT

We investigated the chemical evolution of HC_3N in six dense molecular clouds, using archival available data from the Herschel infrared Galactic Plane Survey (Hi-GAL) and the Millimeter Astronomy Legacy Team Survey at 90 GHz (MALT90). Radio sky surveys of the Multi-Array Galactic Plane Imaging Survey (MAGPIS) and the Sydney University Molonglo Sky Survey (SUMSS) indicate these dense molecular clouds are associated with ultracompact HII (UCHII) regions and/or classical HII regions. We find that in dense molecular clouds associated with normal classical HII regions, the abundance of HC_3N begins to decrease or reaches a plateau when the dust temperature gets hot. This implies UV photons could destroy the molecule of HC_3N . On the other hand, in the other dense molecular clouds associated with UCHII regions, we find the abundance of HC_3N increases with dust temperature monotonously, implying HC_3N prefers to be formed in warm gas. We also find that the spectra of HC_3N (10-9) in G12.804-0.199 and RCW 97 show wing emissions, and the abundance of HC_3N in these two regions increases with its nonthermal velocity width, indicating HC_3N might be a shock origin species. We further investigated the evolutionary trend of $N(\text{N}_2\text{H}^+)/N(\text{HC}_3\text{N})$ column density ratio, and found this ratio could be used as a chemical evolutionary indicator of cloud evolution after the massive star formation is started.

Key words: astrochemistry - stars: formation - ISM: clouds - ISM: abundance

1 INTRODUCTION

Carbon-chain species account for a substantial fraction of the interstellar molecules observed so far. They are prone to be depleted onto dust grains when the gas is cold, and destroyed by UV radiations (Sakai & Yamamoto 2013). In star-forming regions, many carbon-chain species could be used as “chemical clocks” to trace star formation (e.g. Suzuki et al. 1992; Hirota et al. 2009). Cyanopolyynes (HC_{2n+1}N) are one of the representative carbon-chain species. Since the first detection of interstellar cyanoacetylene (HC_3N) by Turner (1971) in Sgr B2, cyanopolyynes have been found to be ubiquitously in our Galactic interstellar medium (ISM) (e.g., Cernicharo & Guélin 1996; Takano et al. 1998; Crovisier et al. 2004). Previously, long chain cyanopolyynes were believed to be abundant in cold dark clouds. In hot cores, they could not be formed efficiently (Millar 1997). However, long chain cyanopolyynes of HC_5N , HC_7N and HC_9N were detected by Sakai et al. (2008) in the protostar IRAS 04368+2557L1527. They proposed a new chemistry called “warm carbon-chain chemistry (WCCC)” in a warm and dense region near the low-mass protostars. Hassell et al. (2008) then made a chemical model of this region. Their calculations show the cyanopolyynes abundance enrichment in the gas phase as the grains warm up to 30 K. Chapman et al. (2009) further presented

that cyanopolyynes could be formed under a hot core condition and show as “chemical clocks” to determine the age of hot cores.

HC_3N is the simplest form of cyanopolyynes. This molecule traces both dense and warm gas. In warm gas, it could be formed from CH_4 (Hassel et al. 2008) and/or C_2H_2 (Chapman et al. 2009) evaporated from grain mantles. Sanhueza et al. (2012) found the median value of HC_3N column density increases as a function of clump evolutionary stage. Taniguchi et al. (2016) observed three ^{13}C isotopologues of HC_3N in L1527 and G28.28-0.36. They found the abundance of H^{13}CCCN and HC^{13}CCN are comparable, while HCC^{13}CN is more abundant. This result could be explained by that HC_3N might be formed from the neutral-neutral reaction between C_2H_2 and CN : $\text{C}_2\text{H}_2 + \text{CN} \rightarrow \text{HC}_3\text{N} + \text{H}$. The abundance of HC_3N can also be enhanced after the passage of shocks. Mendoza et al. (2018) found the abundance of HC_3N increases by a factor of 30 in the shocked region of L1157. Taniguchi et al. (2018) carried out observations of HC_3N and HC_5N toward 52 high-mass star-forming regions with the Nobeyama 45 m telescope. They found the spectra of some HC_3N show wing emissions, suggesting HC_3N is an outflow shock origin species.

The destruction of HC_3N could be caused by UV radiations. Yu & Xu (2016) found the fractional abundances of HC_3N decrease as a function of Lyman continuum fluxes in a number of Red MSX (Midcourse Space Experiment) Sources (RMSs), indicating this molecule could be destroyed by UV photons. Urquhart et al. (2019) conducted a 3-mm molecular line survey towards 570

* E-mail: npyu@bao.ac.cn

ATLASGAL (APEX Telescope Large Area Survey of the Galaxy) clumps. They found the detection rate of HC₃N (10-9) increases from the “Quiescent” stage to the “Protostellar” stage, and reaches a plateau in the “Young Stellar Object (YSOs)” and “HII region” stages. They guess that in the late two stages the formation of HC₃N is in equilibrium with its destruction by UV photons or other chemical reactions. Even to today, there are few researches about chemical evolution of HC₃N in massive star-forming regions. Previous studies mentioned above are surveys of massive clumps/cores in different giant molecular clouds (GMCs). The distances and initial conditions may be quite different in different GMCs. For example, the measured ¹²C/¹³C ratio ranges from ~ 20 to ~ 70, depending on the distance to the Galactic center (e.g. Savage et al. 2002). This might complicate quantitative comparisons and make statistical results not significant. In our previous paper (Yu et al. 2018 hereafter YXW18), we studied the chemical evolution of N₂H⁺ using data from MALT90 and Hi-Gal in six massive star-forming regions. Here we present our study of HC₃N instead of N₂H⁺. The study of other molecules such as C₂H, HCO⁺ and HNC will come in another paper. The distances and initial conditions of clumps could be regarded as the same in the same cloud, and thus a comparison of the chemical evolution in different clumps along the evolutionary sequence is valid. We introduce our data in Section 2, results and discussions are in Section 3, and finally we summarize in Section 4.

2 DATA AND ANALYSIS

Our molecular line data of HC₃N (10-9) comes from MALT90, and the dust infrared data is from Hi-GAL. As the method described by YXW18, we first calculate the H₂ column density and dust temperature maps of these regions, and then the column density and abundance maps of HC₃N. Here we give a brief introduction.

The Hi-GAL data set is comprised of 5 continuum images of the Milky Way Galaxy using the PACS (70 and 160 μm) and SPIRE (250, 350 and 500 μm) instruments. Following the steps described by Wang et al. (2015), we made H₂ column density and dust temperature maps of each region through the method of spectral energy distribution (SED). After removing the background and foreground emissions, we convolved all the images of Hi-GAL to a spatial resolution of 45'', which is the measured beamsize of Hi-GAL observations at 500 μm (Traficante et al. 2011). For each pixel, we use equation

$$I_\nu = B_\nu(1 - e^{-\tau_\nu}) \quad (1)$$

to model intensities at various wavelengths. The optical depth τ_ν could be estimated through

$$\tau_\nu = \mu_{H_2} m_H \kappa_\nu N_{H_2} / R_{gd} \quad (2)$$

We adopt a mean molecular weight per H₂ molecule of $\mu_{H_2} = 2.8$ to include the contributions from Helium and other heavy elements. m_H is the mass of a hydrogen atom. N_{H_2} is the column density. R_{gd} is the gas-to-dust mass ratio which is set to be 100. According to Ossenkopf & Henning (1994), dust opacity per unit dust mass (κ_ν) could be expressed as

$$\kappa_\nu = 5.0 \left(\frac{\nu}{600 \text{GHz}} \right)^\beta \text{cm}^2 \text{g}^{-1} \quad (3)$$

where the value of the dust emissivity index β is fixed to 1.75 in our fitting. The two free parameters (N_{H_2} and T_d) for each pixel could be fitted finally. The final resulting dust temperature and column

density maps, which have a spatial resolution of 45'' with a pixel size of 13'', are shown in Figures 1-6.

MALT90 is an international project with the aim to characterize physical and chemical properties of massive star formation in our Galaxy (e.g., Foster et al. 2011; Foster et al. 2013; Jackson et al. 2013). This project was carried out with the Mopra Spectrometer (MOPS) arrayed on the Mopra 22 m telescope. The beamsize of Mopra is 38'' at 86GHz, with a beam efficiency between 0.49 at 86 GHz and 0.42 at 115 GHz (Ladd et al. 2005). The target of this survey are selected from the ATLASGAL clumps found by Contreras et al. (2013). The image size of each MALT90 data cube is about 4'' × 4'', with a step of 9''. We downloaded the data files from the MALT90 Home Page¹, and assembled all the MALT90 data into a new data cube in a certain region if they have the same velocity component. We have found out six dense molecular clouds showing distinct emissions of HC₃N (10-9). Their infrared images and new combined integrated emissions of HC₃N (10-9) are also shown in Figures 1-6 respectively. All sources involve at least two ATLASGAL clumps. To calculate the abundance of HC₃N in each pixel, we also smoothed the molecular data into a new beamsize of 45'' with a new step of 13''. By assuming local thermodynamic equilibrium (LTE) conditions and HC₃N (10-9) is optically thin, we calculated the HC₃N column density in each pixel where its emission is greater than 5 σ , using the equation from Sanhueza et al. (2012):

$$N = \frac{8\pi\nu^3}{c^3} \frac{Q_{rot}}{g_u A_{ul}} \frac{\exp(E_l/kT_{ex})}{1 - \exp(-h\nu/kT_{ex})} \frac{\int T_{mb} dv}{J(T_{ex}) - J(T_{bg})} \quad (4)$$

where c is the velocity of light in the vacuum, g_u is the statistical weight of the upper level, A_{ul} is the Einstein coefficient for spontaneous transition, E_l is the energy of the lower level, Q_{rot} is the partition function, T_{bg} is the background temperature, T_{ex} is the excitation temperature. Like the assumption make by Sanhueza et al. (2012), we here also assume that T_{ex} is equal to the dust temperature derived above. The values of g_u , A_{ul} and E_l could be found in the Cologne Database for Molecular Spectroscopy (CDMS) (Müller et al. 2001, 2005). $J(T)$ is defined by

$$J(T) = \frac{h\nu}{k} \frac{1}{e^{h\nu/kT} - 1} \quad (5)$$

For the uncertainties of column density, here we only consider the errors from its integrated intensities. We should mention here that to calculate the column density of HC₃N, we made an assumption that the HC₃N (10-9) line is optically thin. The true column density derived by Eq. (4) should be multiplied by a factor of $\tau / (1 - e^{-\tau})$. For an intermediately optically thick line (τ : 0.5 ~ 2), the true column density will be higher by a factor of 1.3 to 2.3 for our sources. The abundance value of HC₃N ($\chi(\text{HC}_3\text{N})$) for each pixel can be calculated through $\chi(\text{HC}_3\text{N}) = N(\text{HC}_3\text{N})/N(\text{H}_2)$ finally. The HC₃N abundance maps for each source are shown in Figures 7-12.

3 INDIVIDUAL SOURCES AND DISCUSSIONS

3.1 G5.899-0.429

The dense cloud G5.899-0.429 involves 5 ATLASGAL clumps. Four of them have been observed by MALT90 (Figure 1, the green boxes). The distance of this cloud is about 2.9 kpc (Sato et al.

¹ <http://atoa.atnf.csiro.au/MALT90>

2014). From Figure 1, we can see that the HC_3N (10-9) emission is very compact and comes from the densest part of this cloud. The most massive clump AGAL005.884-00.392, which has the strongest emission of HC_3N , is also known as an expanding UCHII region W28 A2 (Wood & Churchwell 1989). The expanding velocity of this UCHII regions is about 35 km s^{-1} (Acord et al. 1998). Near infrared observations indicate the exciting source of this UCHII region is a young O-type star (Feldt et al. 2003). Zapata et al. (2019) carried out high angular resolution observations and found an explosive outflow from this UCHII region. The south-east part of this cloud involves two ATLASGAL clumps which show relatively weak emissions of HC_3N (10-9). The 90 cm radio continuum emissions from MAGPIS are shown in yellow contours in the top left panel of Figure 1. We can see that radio emissions here are more diffuse and larger than that in the UCHII region, indicating this might be a normal classical HII region. From Figure 7, we can see that compared to the south-east part, $\chi(\text{HC}_3\text{N})$ is more abundant in the UCHII region, and the abundance of HC_3N increases with dust temperature monotonously in the whole region. The spectra of HCO^+ (1-0) shows the so-called “blue profile” with extended wing emissions where the $\chi(\text{HC}_3\text{N})$ is highest, indicating star-forming activities such as infall and outflow. This result suggests that HC_3N prefers to be formed in warm gas with massive star-forming activities.

3.2 G12.804-0.199

This dense molecular cloud is associated with the well-known GMC W33. The distance of W33 is about 2.4 kpc (Immer et al. 2013). It includes three large dust clumps (W33 Main, W33 A and W33 B) and three smaller clumps (W33 Main1, W33 A1 and W33 B1). Even though these clumps are involved in a whole star-forming complex, radio line observations found W33 Main and W33 A have a radial velocity of $\sim 36 \text{ km s}^{-1}$, while W33 B has a different radial velocity of $\sim 58 \text{ km s}^{-1}$. Using molecular line data from MALT90, we checked both the two velocity components, only founding HC_3N (10-9) emissions in W33 Main and W33 A (see the top right panel of Figure 2). The 90 cm radio continuum emissions from MAGPIS in Figure 2 show W33 Main as a compact source, which is also known to be an UCHII region (Keto & Ho 1989). On the south-east of W33 Main, there is a strong arc-shaped radio emission. Ho et al. (1986) suggest this is an ionization front penetrating W33 Main. The HCO^+ (1-0) spectra in W33 Main also shows the so-called “blue profile” with extended wing emissions (Figure 8), indicating infall and outflow activities in W33 Main. We do not found radio emission in the center of W33 A. However, van der Tak & Menten (2005) found faint 43 GHz radio emissions in W33 A with higher resolution observations. They suggest the faint emissions come from an ionised wind or a hypercompact HII region (HCHII) in W33 A. Immer et al. (2014) detected a large number of simple and complex molecules in W33 A. They suggest W33 A may be in the transition from the hot core stage to the HCHII region phase. Thus W33 Main is more evolved than W33 A. From Figure 8, we can see that HC_3N is more abundant in W33 Main than that in W33 A. Like that found in G5.899-0.429, the abundance of HC_3N also increases with dust temperature in G12.804-0.199. This result also suggests that HC_3N prefers to be formed in warm gas with massive star-forming activities.

3.3 G326.641+0.612 (RCW 95)

The dense molecular cloud G326.641+0.612 is associated with the classical HII region RCW 95 (Rodgers et al. 1960). The kinematic distance of RCW 95 is about 2.4 kpc (Giveon et al. 2002). YXW18 found that in this region the abundance of N_2H^+ reaches a plateau as the dust temperature is above 27 K (see their Figure 10). They thus suggest the destruction of N_2H^+ by CO or UV photons around this classical HII region. From Figure 9, we can see that as the dust temperature gets hot, the abundance of HC_3N also seems to reach a plateau, indicating the destruction of HC_3N by UV photons.

3.4 G327.293-0.579 (RCW 97)

The dense molecular cloud G327.293-0.579 is associated with a luminous photon dominated region (PDR) around the classical HII region RCW 97 on the north side, and an IRDC on the south side (Wyrowski et al. 2006). From Figure 4, we can see that the emission of HC_3N (10-9) mainly comes from the IRDC which hosts the hot core G327.3-0.6 (Gibbet al. 2000) and extended green object (EGO) candidate G327.30-0.58 (Cyganowski et al. 2008). Assuming a kinematic distance of 3.0 kpc (Russeil 2003), the Lyman continuum flux from RCW97 will be more than $10^{50} \text{ photons s}^{-1}$ (Conti & Crowther 2004), indicating this is a giant HII region. Both infall and outflow activities have been found by Leurini et al. (2017) in the IRDC. From Figure 10, it can be noticed that the abundance of HC_3N is highest in the IRDC, and begins to drop as the dust temperature gets hotter than 30 K. This is also consistent with the scenario that HC_3N could be destroyed by UV photons.

3.5 G337.916-0.477 (S36)

This dense molecular cloud is associated with the infrared bubble S36 (Churchwell et al. 2006). The radio continuum emissions from SUMSS shown in Figure 5 indicate this is also a classical HII region. YXW18 found that in this region, the abundance of N_2H^+ increases with dust temperature when it is below 28 K, and then decreases quickly in the PDR where T_d is hotter than 28 K (also see their Figure 10). From Figure 11, we can see that the situation of HC_3N is similar to that of N_2H^+ in this region, indicating UV photons are also destroying HC_3N and N_2H^+ on the PDR of S36.

3.6 G345.448+0.314

The dense molecular cloud G345.448+0.314 involves two ATLASGAL clumps. The two clumps are associated with IRAS 17008-4040 and IRAS 17009-4042 respectively. The radio continuum emissions from SUMSS in Figure 6 indicate HII regions in these two clumps. Using high resolution archival data from the Giant Metrewave Radio Telescope (GMRT), Dewangan et al. (2018) found 13 HII regions with radius in the range of 0.06 pc and 0.25 pc in these two IRAS sources. The radius of these HII regions indicate they are still in the UCHII stage. Like those found in G5.899-0.429 and G12.804-0.199 introduced above, the abundance of HC_3N also increases with dust temperature (Figure 12), indicating the production of HC_3N is more efficient than its destruction here. This may be because compared to classical HII regions, UCHII regions are still surrounded by dense gas, providing shielding against UV radiation. The spectra of HCO^+ (1-0) shows red and blue profiles with wing emissions in IRAS 17008-4040 and IRAS 17009-4042, indicating star-forming activities in this dense molecular cloud. Like

that found in the other UCHII regions (G5.899-0.429 and G12.804-0.199) above, this result also suggests that HC₃N prefers to be formed in warm gas with massive star-forming activities.

3.7 Discussions

We found that in dense molecular clouds associated with classical HII regions (RCW 95, RCW 97 and infrared bubble S36), the abundance of HC₃N does not increase with dust temperature monotonously. It begins to decrease or reaches a plateau as the dust temperature gets hot. In a previous paper (Yu & Xu 2016), we also found that the abundance of HC₃N decreases with Lyman continuum flux. These studies indicate that HC₃N can be destroyed by UV radiation. Chemical network from KIDA² (Wakelam et al. 2014) tells us that HC₃N could be destroyed through reaction: HC₃N + Photon → CN + C₂H and/or HC₃N + Photon → HC₃N⁺ + e⁻. Besides, UV photons could also destroy C₂H₂ which is the main progenitor of HC₃N through reaction: C₂H₂ + Photon → C₂H + H, leading to the production of HC₃N ineffective.

On the other hand, the situation was quite different in UCHII regions of G5.899-0.429, G12.804-0.199 and G345.448+0.14. We found that in these regions, the abundance of HC₃N increases with dust temperature. This may be because that in warm gas the progenitors of HC₃N (such as C₂H₂ and CH₄) could be easily released into gas phase. Yu & Wang (2015) found that in massive young stellar objects (MYSOs), the line widths of HC₃N are comparable to those of N₂H⁺, which is regarded as a good tracer of cold dense gas. However, in UCHII regions the line widths of HC₃N become broader than those of N₂H⁺. Taniguchi et al. (2018) also found that the line widths of HC₃N are significantly broader than those of HC₃N. These studies indicate HC₃N prefers to exist in more active star-forming regions. From Figure 7, 8, 10 and 12, we can see that the spectra of HCO⁺ (1-0) show red and blue profiles with wing emissions where the abundance of HC₃N is highest. Previous multi-wavelength observations also indicate shock activities (caused by infall, outflow and/or expanding HII regions) in these regions. We also checked the spectra of HC₃N (10-9) in these regions, and found that in G12.804-0.199 and RCW 97 the spectra of HC₃N (10-9) show wing emissions (Figure 13). This suggests HC₃N might be an outflow shock origin species. The abundance of HC₃N could be increased in the passage of shocks. The chemical model of Mendoza et al. (2018) shows that the abundance of HC₃N could be directly increased due to mantle sputtering due to the passage of shocks. Besides, their model also indicates shock activities could increase the reaction efficiency of CN with C₂H₂: C₂H₂ + CN → HC₃N + H.

The velocity dispersion of HC₃N (10-9) caused by thermal motions could be estimated by:

$$\Delta V_{therm} = \sqrt{8 \ln 2 k T_d \left(\frac{1}{m_{HC_3N}} + \frac{1}{m} \right)} \quad (6)$$

where m_{HC_3N} is the mass of HC₃N (51 per amu), m is the mean molecular mass (2.3 per amu). Figure 13 shows the relationship between the abundance of HC₃N and its nonthermal line widths ($\Delta V_{nontherm}^2 \equiv \Delta V_{FWHM}^2 - \Delta V_{therm}^2$) in G12.804-0.199 and RCW 97. It can be noticed that the abundance of HC₃N increases with its nonthermal line width in these two regions. This result also suggests that HC₃N could be efficiently formed by massive star formation

activities. We thus regard that HC₃N prefers to be formed in warm gas with massive star-forming activities. We suggest more line observations with higher resolutions to be carried out to find out the chemical evolution of HC₃N in massive star-forming regions.

Previous studies of low-mass star-forming regions suggest the ratio of $N(\text{nitrogen-bearing species})/N(\text{carbon-chain species})$ increases as a cloud evolves (e.g. Suzuki et al. 1992; Benson et al. 1998; Hirota et al. 2009). Suzuki et al. (1992) carried out observations of CCS, HC₃N, HC₅N and NH₃ toward 49 dark cloud cores in the Taurus and Ophiuchus regions. They found carbon-chain molecules like CCS are abundant in the early stages of chemical evolution, while NH₃ is abundant in the later stages. They suppose that in the early stages of star formation, carbon-chain molecules could be efficiently formed from ionic carbon (C⁺) and atomic carbon (C). However, as the cloud evolves further, the formation efficiency of carbon-chain molecules decrease, because most of the carbon atoms are converted into the form of CO, which is chemically stable. On the other hand, nitrogen-bearing species such as NH₃ become gradually abundant in the central part of the core. Thus the abundance ratio of CCS and NH₃ could be used as a good indicator of cloud evolution and star formation. Benson et al. (1998) made a high spatial resolution observation of N₂H⁺, C₃H₂ and CCS toward 60 dense cores. They found that the ratio of $N(\text{CCS})/N(\text{N}_2\text{H}^+)$ in starless cores is higher by a factor of 2 than that in cores with stars. This result is consistent with the finding of Suzuki et al. (1992). Ohashi et al. (2014; 2016) have investigated molecular lines of HC₃N (10-9) and N₂H⁺ (1-0) in the cluster forming regions of Orion A and Vela C GMCs. They found that the ratios of $N(\text{NH}_3)/N(\text{CCS})$ and $N(\text{N}_2\text{H}^+)/N(\text{HC}_3\text{N})$ could also be the tracers of the chemical evolution even in the high mass star forming region in the same way as the low mass star forming region. Figure 14 shows the relationship between $N(\text{N}_2\text{H}^+)/N(\text{HC}_3\text{N})$ and T_{dust} in all of our sources. It can be noticed that in all sources, the relative column density ratios of N₂H⁺ and HC₃N do not increase with dust temperature. Moreover, in G5.899-0.429, G12.804-0.199, RCW 97, S36 and G345.448+0.314, it is clear that this ratio decreases as dust temperature increases, which is totally different to that found by Ohashi et al. (2016). The reason may be that we focused on the different evolutionary stages of massive star formation. It is generally accepted that massive stars evolve from starless cores in IRDCs to hot cores with central young stellar objects, then to HCHII and UCHII regions. The final stages are compact and classical HII regions (Zinnecker et al. 2007). Previous studies of Ohashi et al. (2016) compared starless cores with star-forming (Class 0/I) sources. In this work, we focused on sources of UCHII regions and classical HII regions, where massive protostars have already formed. According to the new chemistry of WCCC, Sakai et al. (2008) suggested that the HC₃N will be more enhanced after star formation starts due to the evaporation from the grain surface. The increase of $\chi(\text{HC}_3\text{N})$ with dust temperature has been founded in G5.899-0.429 (Figure 7), G12.804-0.199 (Figure 8) and G345.448+0.314 (Figure 12), and the decrease of $\chi(\text{N}_2\text{H}^+)$ with dust temperature in S36 has also been shown in our previous paper of YXW18. This may be the reason that the ratio of $N(\text{N}_2\text{H}^+)/N(\text{HC}_3\text{N})$ decreases with the dust temperature in our sources. Our study suggests this ratio still could be used as a chemical evolutionary indicator of cloud evolution after the massive star formation is started.

² <http://kida.obs.u-bordeaux1.fr/>

4 SUMMARY

We investigate the chemical evolution of HC₃N in six dense molecular clouds, using data from MALT90 and Hi-GAL. Radio sky surveys indicate these dense molecular clouds are associated with UCHII regions and/or classical HII regions. We found that in dense molecular clouds associated with classical HII regions, the abundance of HC₃N decreases or reaches a plateau when the dust temperature gets hot, implying UV photons could destroy the molecule of HC₃N. On the other hand, in dense molecular clouds associated with UCHII regions, we found the abundance of HC₃N increases with dust temperature monotonously. The spectra of HCO⁺ (1-0) and HC₃N (10-9) in some sources show wing emissions. We also found that the abundance of HC₃N increases with its nonthermal velocity width in G12.804-0.199 and RCW 97. These results suggest HC₃N prefers to be formed in warm gas with star-forming activities, and could be destroyed by UV photons in the late stages of massive star formation. We also found that in most sources, the column density ratio of N₂H⁺ and HC₃N decreases with the dust temperature. Our study seems to support that the column density ratio of N₂H⁺ and HC₃N could still be used as a chemical evolutionary indicator of cloud evolution after the massive star formation is started.

5 ACKNOWLEDGEMENTS

We thank the anonymous referee for constructive suggestions. This paper has made use of information from the ATLASGAL Database Server³. The ATLASGAL project is a collaboration between the Max-Planck-Gesellschaft, the European Southern Observatory (ESO) and the Universidad de Chile. This research made use of data products from the Millimetre Astronomy Legacy Team 90 GHz (MALT90) survey. The Mopra telescope is part of the Australia Telescope and is funded by the Commonwealth of Australia for operation as National Facility managed by CSIRO. This paper is supported by the Youth Innovation Promotion Association of CAS.

REFERENCES

- Acord J. M., Churchwell E., Wood D. O. S. 1998, *ApJ*, 495, L107
Benson P. J., Caselli P., & Myers P. C. 1998, *ApJ*, 506, 743
Cernicharo J., Guélin M. 1996, *A&A*, 309, L27
Chapman J. F., Millar T. J., Wardle M., Burton M. G., Walsh A. J. 2009, *MNRAS*, 394, 221
Churchwell, E., Povich, M. S., Allen, D., et al. 2006, *ApJ*, 649, 759
Conti P. S., Crowther P. A. 2004, *MNRAS*, 355, 899
Contreras Y., Schuller F., Urquhart J. S., et al. 2013, *A&A*, 549, A45
Crovisier J. et al. 2004, *A&A*, 418, 1141
Cyrowski C. J., Whitney B. A., Holden E. et al. 2008, *AJ*, 136, 2391
Dewangan L. K., Baug T., Ojha D. K., Ghosh S. K. 2018, *ApJ*, 869, 30
Feldt M., Puga, E., Lenzen, R. et al. 2003, *ApJ*, 599, L91
Foster J. B., Jackson J. M., Barnes P. J. et al. 2011, *ApJS*, 197, 25
Gibb E., Nummelin A., Irvine W. M., Whittet D. C. B., Bergman P. 2000, *ApJ*, 545, 309
Giveon A., Sternberg A., Lutz D., Fruchtgruber H., Pauldrach, A. W. A. 2002, *ApJ*, 566, 880
Hassel G. E., Herbst E., Garrod R. T. 2008, *ApJ*, 681, 1385
Hirota T. Ohishi M. & Yamamoto S. 2009, *ApJ*, 699, 585
Ho P. T. P., Klein R. I., Haschick A. D. 1986, *ApJ*, 305, 714
Immer K., Reid M. J., Menten K. M., Brunthaler A., Dame T. M. 2013, *A&A*, 553, A117
Immer K., Galván-Madrid R., König C., Liu H. B., Menten K. M. 2014, *A&A*, 572, A63
Jackson, J. M., Rathborne, J. M., Foster, J. B., et al. 2013, *PASA*, 30, 57
Keto E. R., & Ho P. T. P. 1989, *ApJ*, 347, 349
Ladd, N., Purcell, C., Wong, T., & Robertson, S. 2005, *PASA*, 22, 62
Lada C. J., Lombardi M., & Alves J. F. 2010, *ApJ*, 724, 687
Leurini S., Herpin F., van der Tak F., Wrowski F., Herczeg G. J., van Dishoeck E. F. 2017, *A&A*, 602, A70
Mendoza E., Lefloch B., Ceccarelli C. et al. 2018, *MNRAS*, 475, 5501
Millar T. J., Macdonald G. H., Gibb A. G. 1997, *A&A*, 325, 1163
Müller H. S. P., Thorwirth S., Roth D. A., & Winnewisser G. 2001, *A&A*, 370, L49
Müller H. S. P., Schlöder F., Stutzki J., & Winnewisser G. 2005, *J. Molec. Struct.*, 742, 215
Ohashi S., Tatematsu K., Choi M., et al. 2014, *PASJ*, 66, 119
Ohashi S., Tatematsu K., Fujii K., et al. 2016, *PASJ*, 68, 3
Ossenkopf V., Henning T., 1994, *A&A*, 291, 943
Rathborne J. M., Whitaker J. S., Jackson J. M., et al. 2016, *Publ. Astron. Soc. Aust.*, 33, e030
Rodgers A. W., Campbell C. T., & Whiteoak J. B. 1960, *MNRAS*, 121, 103
Russeil D. 2003, *A&A*, 397, 133
Sakai N. Sakai T. Hirota T. Yamamoto S. 2008 *ApJ*, 672, 371
Sakai N., & Yamamoto S. 2013, *ChRv*, 113, 8981
Sanhueza, P., Jackson, J. M., Foster, J. B., Garay, G., Silva, A., Finn, S. C., 2012, *ApJ*, 756, 60
Sato M., Wu Y. W., Immer K., et al. 2014, *ApJ*, 793, 72
Suzuki H., Yamamoto S., Ohishi M. et al. 1992, *ApJ*, 392, 551
Taniguchi K., Saito M., Ozeki H. 2016, *ApJ*, 830, 106
Taniguchi K., Saito M., Sridharan T. K., Minamidani T. 2018, *ApJ*, 854, 133
Taniguchi K., Saito M., Sridharan T. K., Minamidani T. 2019, *ApJ*, 872, 154
Takano S., et al. 1998, *A&A*, 329, 1156
Traficante, A., Calzoletti, L., Veneziani, M., et al. 2011, *MNRAS*, 416, 2932
Turner B. E. 1971, *ApJ*, 163, L35
Urquhart J. S., Figura C., Wyrowski F., et al. 2019, *MNRAS*, 484, 4444
van der Tak F. F. S., & Menten K. M. 2005, *A&A*, 437, 947
Wakelam V., Vastel C., Aikawa Y., et al. 2014, *MNRAS*, 445, 2854
Wang, K., Testi, L., Ginsburg, A., et al. 2015, *MNRAS*, 450, 4043
Wood D. O., Churchwell E. 1989, *ApJS*, 69, 831
Wyrowski F., Menten K. M., Schilke P., et al. 2006, *A&A*, 454, L91
Yamamoto T., Nakagawa N., & Fukui Y. 1983, *A&A*, 122, 171
Yu N. P., & Wang J. J. 2015, *MNRAS*, 451, 2507
Yu N. P., & Xu J. L. 2016, *ApJ*, 833, 248
Yu N. P., Xu J. L., Wang J. J., Liu X. L. 2018, *ApJ*, 865, 135
Zapata L. A., Ho P. T. P., Guzmán E. et al. 2019, *arXiv:1904.04385*

³ http://atlasgal.mpifr-bonn.mpg.de/cgi-bin/ATLASGAL_DATABASE.cgi

Zinnecker H., Yorke H. W., 2007, ARA&A, 45, 481

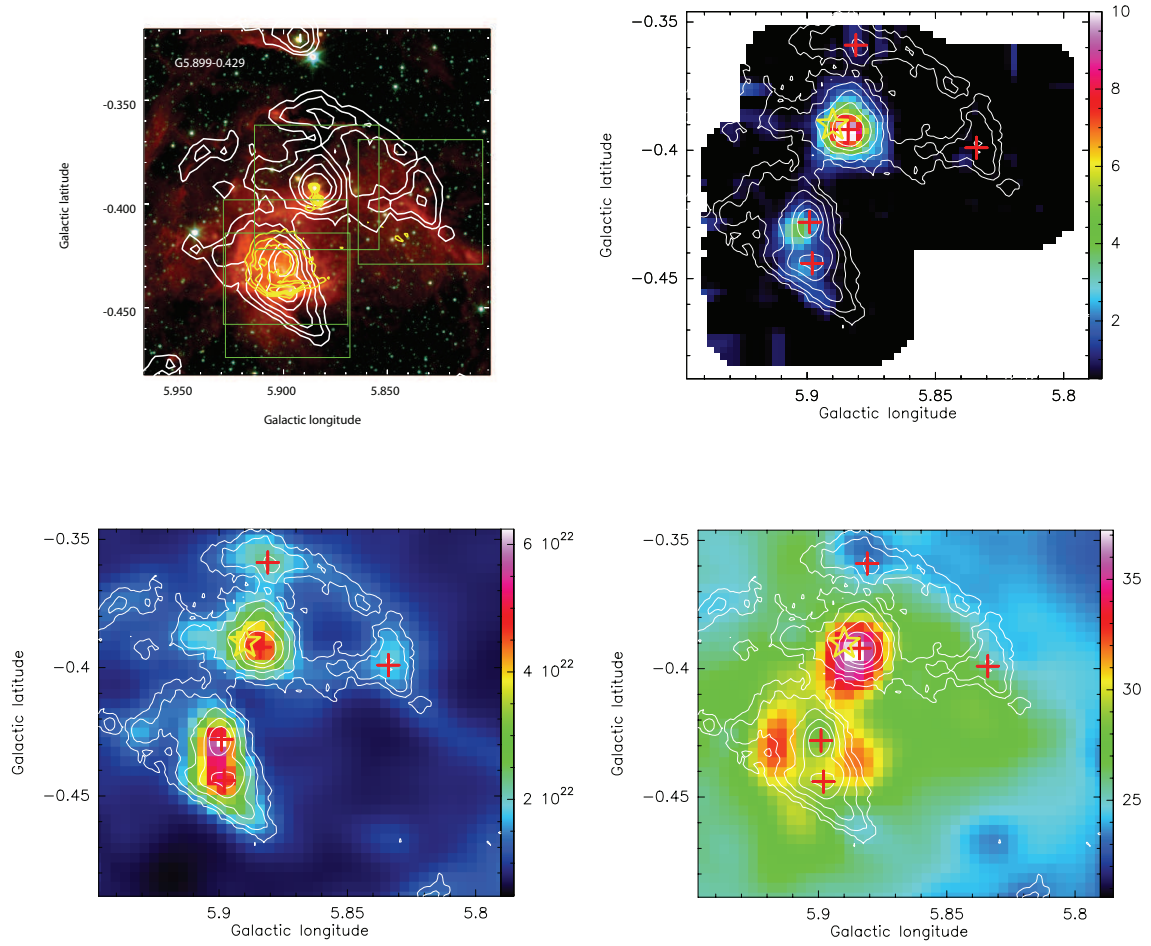


Figure 1. Top left: Three colour mid-infrared image of G5.899-0.429 created using the Spitzer IRAC band filters ($8.0\ \mu\text{m}$ in red, $4.5\ \mu\text{m}$ in green and $3.6\ \mu\text{m}$ in blue). The green boxes indicate the four observed regions by MALT90. Top right: The new combined image of HC_3N from MALT90 data set. The emission has been integrated from 3 to $15\ \text{km s}^{-1}$. The unit of the color bar on the right is in K km/s . Bottom left: The H_2 column density of this region built through SED fitting. The unit of color bar is in cm^{-2} . Bottom right: The dust temperature map in color scale derived from the SED fitting. The unit of color bar is in K . The ATLASGAL $870\ \mu\text{m}$ emissions (in white) are superimposed with levels 0.24 , 0.48 , 0.96 , 1.92 and $3.84\ \text{Jy/beam}$ in each panel. The red pluses mark the center locations of ATLASGAL clumps. The yellow star marks the UCHII region W28 A2. The $90\ \text{cm}$ radio continuum emissions (in yellow) from MAGPIS are superimposed with levels 0.1 , 0.2 , 0.3 , 0.4 , and $0.5\ \text{Jy beam}^{-1}$.

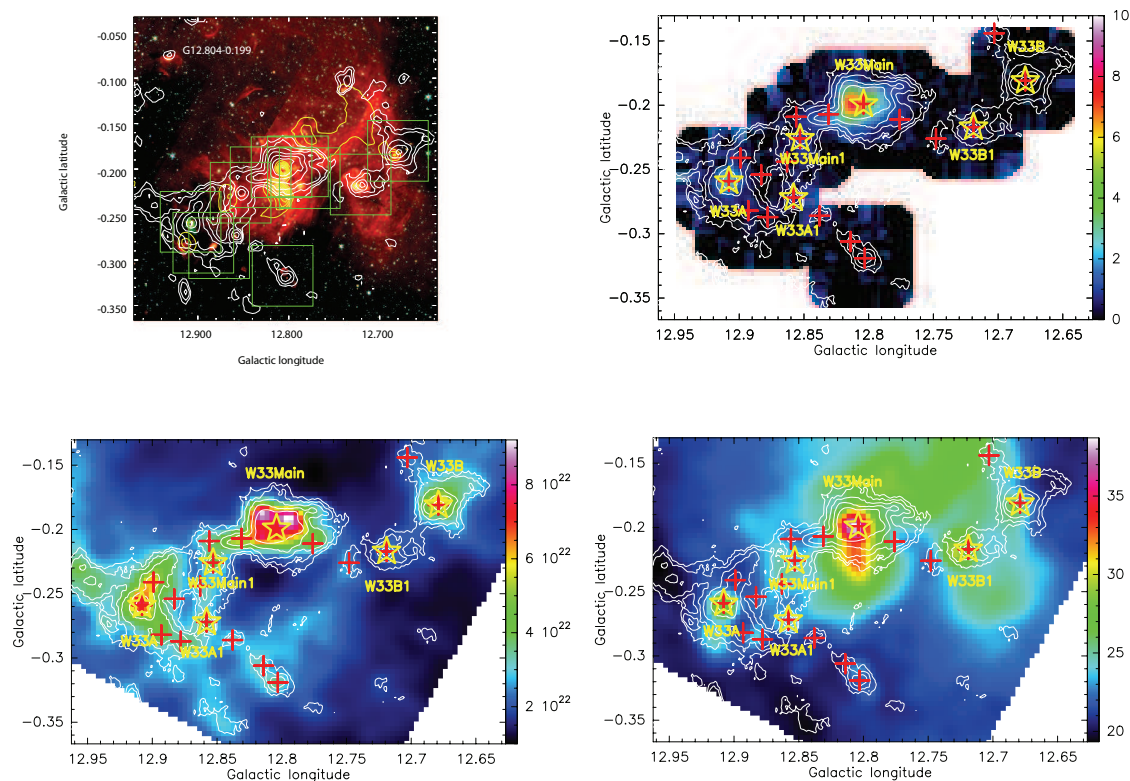


Figure 2. Top left: Three colour mid-infrared image of G12.804-0.199 created using the Spitzer IRAC band filters ($8.0 \mu\text{m}$ in red, $4.5 \mu\text{m}$ in green and $3.6 \mu\text{m}$ in blue). The green boxes indicate the observed regions by MALT90. Top right: The new combined image of HC_3N from MALT90 data set. The emission has been integrated from 30 to 40 km s^{-1} . The unit of the color bar on the right is in K km/s . Bottom left: The H_2 column density of this region built through SED fitting. The unit of color bar is in cm^{-2} . Bottom right: The dust temperature map in color scale derived from the SED fitting. The unit of color bar is in K . The ATLASGAL $870 \mu\text{m}$ emissions (in white) are superimposed with levels $0.24, 0.48, 0.96, 1.92, 3.84$ and 7.68 Jy/beam in each panel. The red pluses mark the center locations of ATLASGAL clumps. The yellow stars mark W33A, W33A1, W33Main1, W33Main, W33B1 and W33B. The 90 cm radio continuum emissions (in yellow) from MAGPIS are superimposed with levels $0.02, 0.04, 0.08, 0.16,$ and $0.32 \text{ Jy beam}^{-1}$.

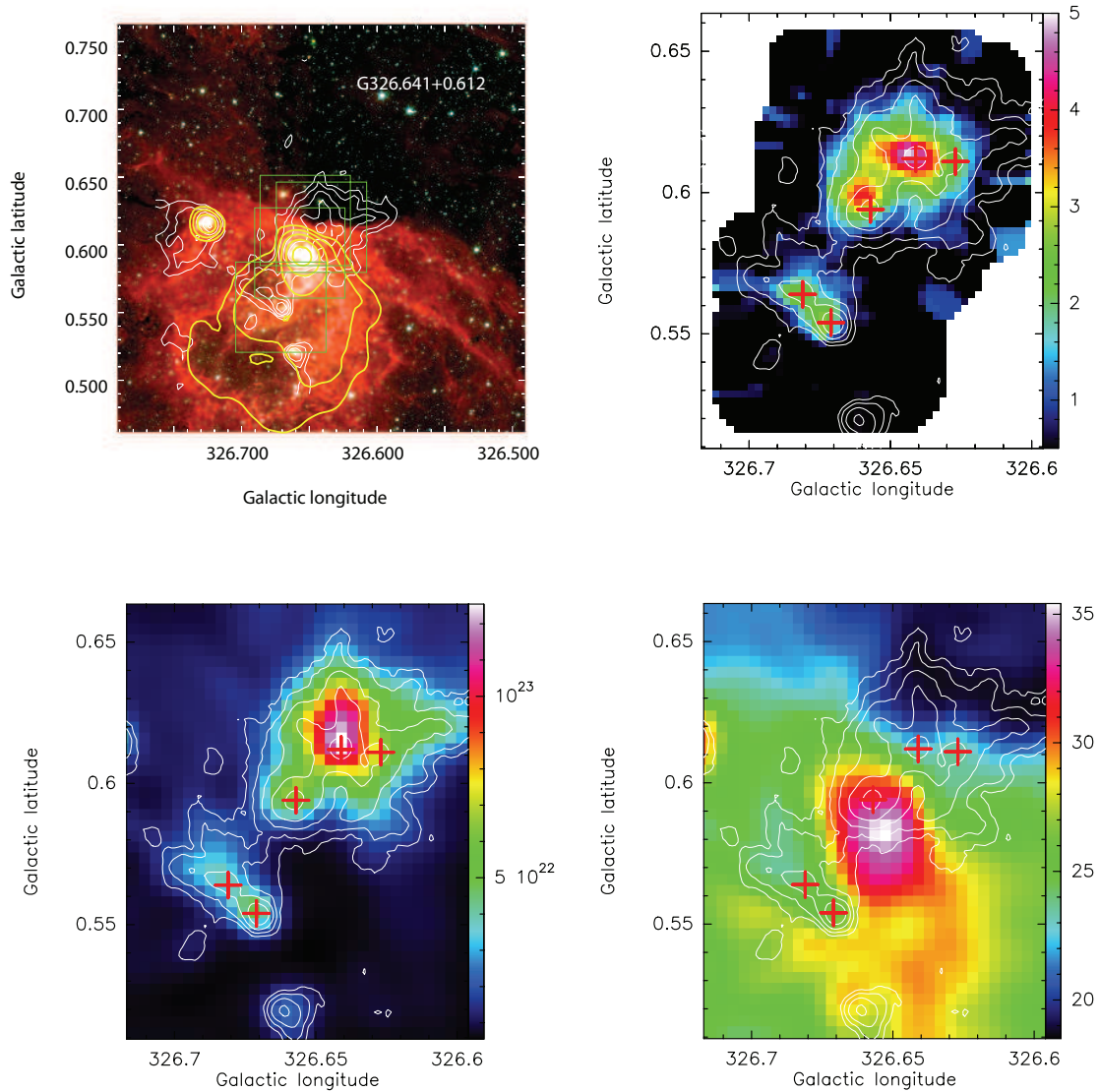


Figure 3. Top left: Three colour mid-infrared image of G326.641+0.612 created using the Spitzer IRAC band filters ($8.0 \mu\text{m}$ in red, $4.5 \mu\text{m}$ in green and $3.6 \mu\text{m}$ in blue). The green boxes indicate the four observed regions by MALT90. Top right: The new combined image of HC_3N from MALT90 data set. The emission has been integrated from -44 to -36 km s^{-1} . The unit of the color bar on the right is in K km/s . Bottom left: The H_2 column density of this region built through SED fitting. The unit of color bar is in cm^{-2} . Bottom right: The dust temperature map in color scale derived from the SED fitting. The unit of color bar is in K . The ATLASGAL $870 \mu\text{m}$ emissions (in white) are superimposed with levels 0.42, 0.84, 1.68, 3.36, and 6.72 Jy/beam in each panel. The red pluses mark the center locations of ATLASGAL clumps. The 843 MHz SUMSS radio continuum emissions (in yellow) are superimposed with levels 0.2, 0.4, 0.8, 1.6, and 3.2 Jy beam^{-1} .

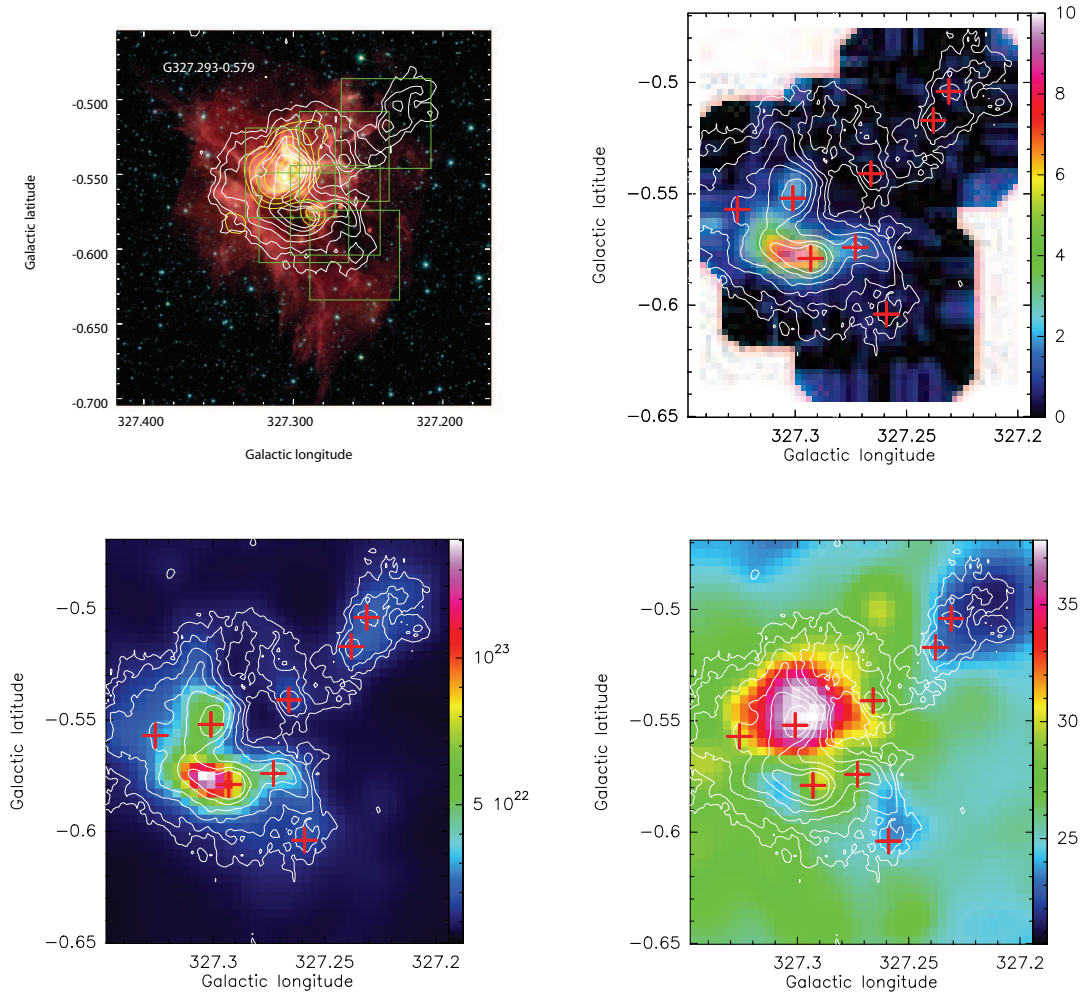


Figure 4. Top left: Three colour mid-infrared image of G327.293-0.579 created using the Spitzer IRAC band filters ($8.0\ \mu\text{m}$ in red, $4.5\ \mu\text{m}$ in green and $3.6\ \mu\text{m}$ in blue). The green boxes indicate the five observed regions by MALT90. Top right: The new combined image of HC_3N from MALT90 data set. The emission has been integrated from -50 to $-41\ \text{km s}^{-1}$. The unit of the color bar on the right is in K km/s . Bottom left: The H_2 column density of this regions built through SED fitting. The unit of color bar is in cm^{-2} . Bottom right: The dust temperature map in color scale derived from the SED fitting. The unit of color bar is in K . The ATLASGAL $870\ \mu\text{m}$ emissions (in white) are superimposed with levels 0.21, 0.42, 0.84, 1.68, 3.36, and $6.72\ \text{Jy/beam}$ in each panel. The red pluses mark the center locations of ATLASGAL clumps. The 843 MHz SUMSS radio continuum emissions (in yellow) are superimposed with levels 0.3, 0.6, 1.2, 2.4, and $4.8\ \text{Jy beam}^{-1}$.

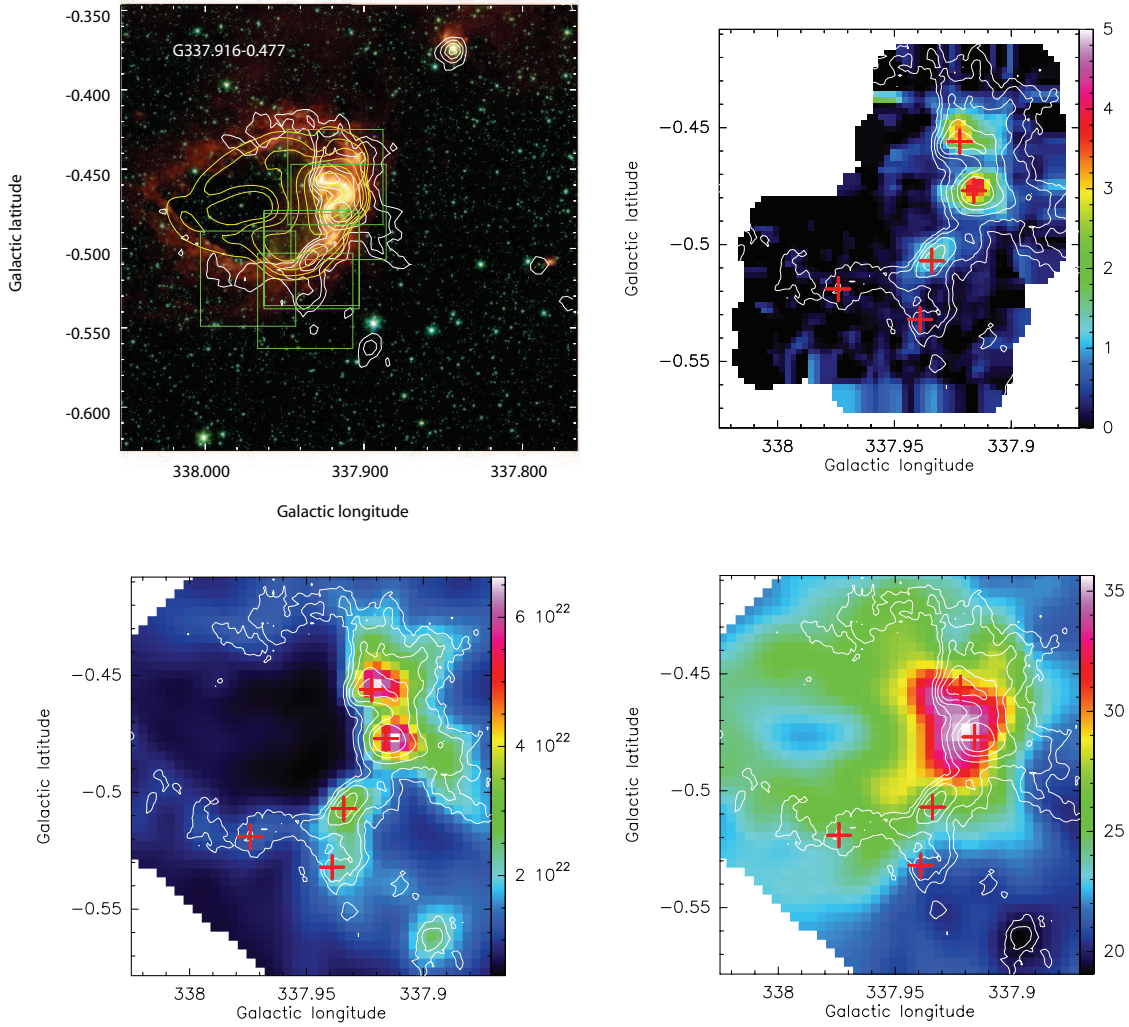


Figure 5. Top left: Three colour mid-infrared image of G337.916-0.477 created using the Spitzer IRAC band filters ($8.0\ \mu\text{m}$ in red, $4.5\ \mu\text{m}$ in green and $3.6\ \mu\text{m}$ in blue). The green boxes indicate the six observed regions by MALT90. Top right: The new combined image of HC_3N from MALT90 data set. The emission has been integrated from -42 to $-37\ \text{km s}^{-1}$. The unit of the color bar on the right is in K km/s . Bottom left: The H_2 column density of this regions built through SED fitting. The unit of color bar is in cm^{-2} . Bottom right: The dust temperature map in color scale derived from the SED fitting. The unit of color bar is in K . The ATLASGAL $870\ \mu\text{m}$ emissions (in white) are superimposed with levels 0.27, 0.54, 1.08, 2.16, and $4.32\ \text{Jy/beam}$ in each panel. The red pluses mark the center locations of ATLASGAL clumps. The 843 MHz SUMSS radio continuum emissions (in yellow) are superimposed with levels 0.05, 0.10, 0.20, 0.40, 0.80, 1.60 and $3.20\ \text{Jy beam}^{-1}$.

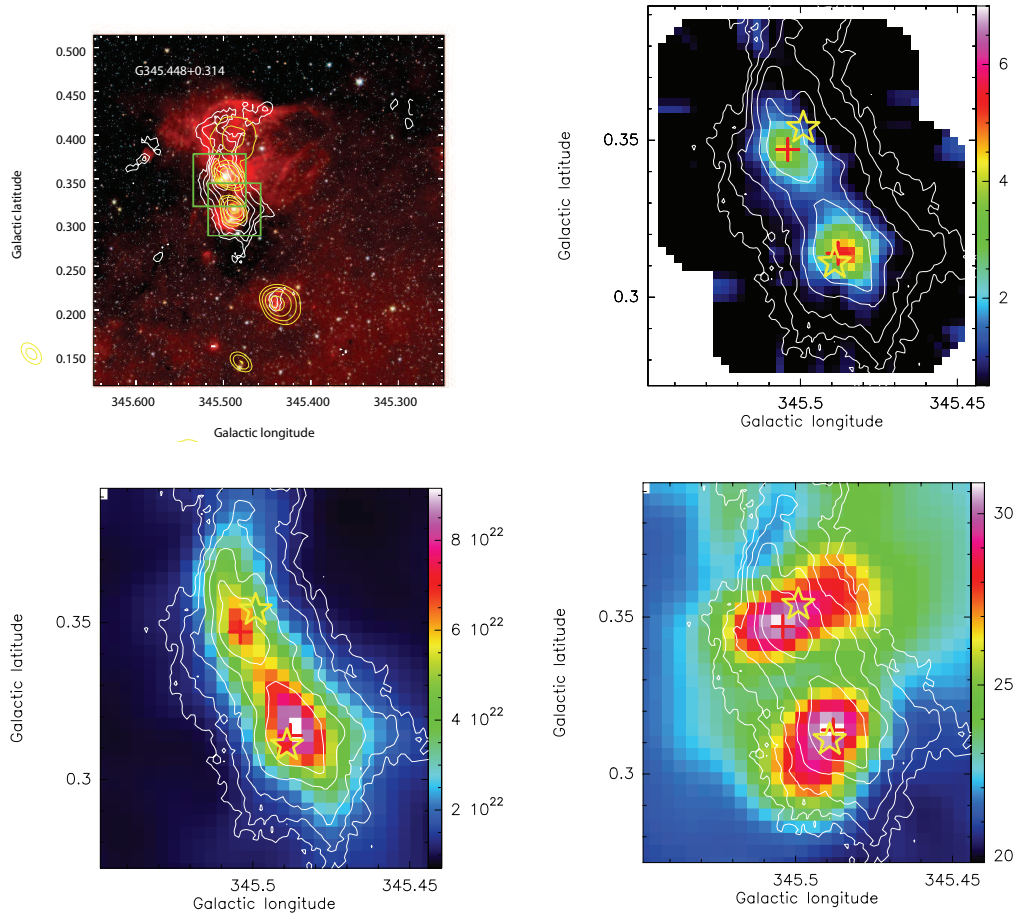


Figure 6. Top left: Three colour mid-infrared image of G345.448+0.314 created using the Spitzer IRAC band filters ($8.0\ \mu\text{m}$ in red, $4.5\ \mu\text{m}$ in green and $3.6\ \mu\text{m}$ in blue). The green boxes indicate the two observed regions by MALT90. Top right: The new combined image of HC_3N from MALT90 data set. The emission has been integrated from -21 to $-14\ \text{km s}^{-1}$. The unit of the color bar on the right is in K km/s . Bottom left: The H_2 column density of this regions built through SED fitting. The unit of color bar is in cm^{-2} . Bottom right: The dust temperature map in color scale derived from the SED fitting. The unit of color bar is in K . The ATLASGAL $870\ \mu\text{m}$ emissions (in white) are superimposed with levels 0.18, 0.36, 0.72, 1.44, and 2.88 Jy/beam in each panel. The red pluses mark the center locations of ATLASGAL clumps. The two yellow stars mark IRAS 17008-4040 and IRAS 17009-4042. The 843 MHz SUMSS radio continuum emissions (in yellow) are superimposed with levels 0.02, 0.04, 0.08, and 0.16 Jy beam^{-1} .

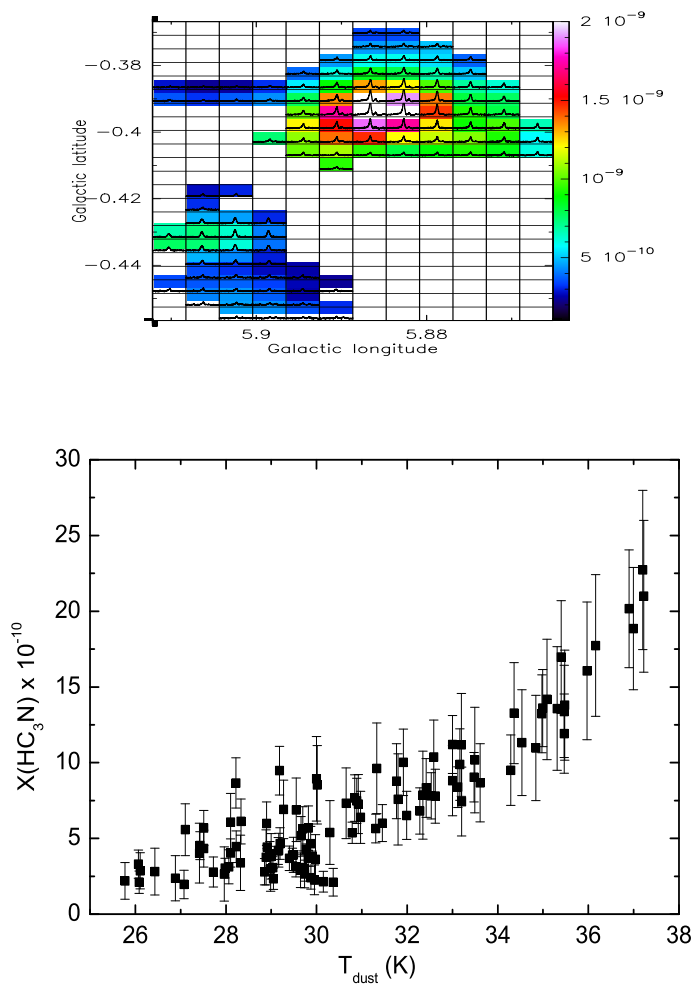


Figure 7. Top: The HCO⁺ (1-0) spectra superimposed on the calculated HC₃N abundance map of G5.899-0.429. Bottom: Abundance of HC₃N plotted as a function of the dust temperature in each pixel of G5.899-0.429.

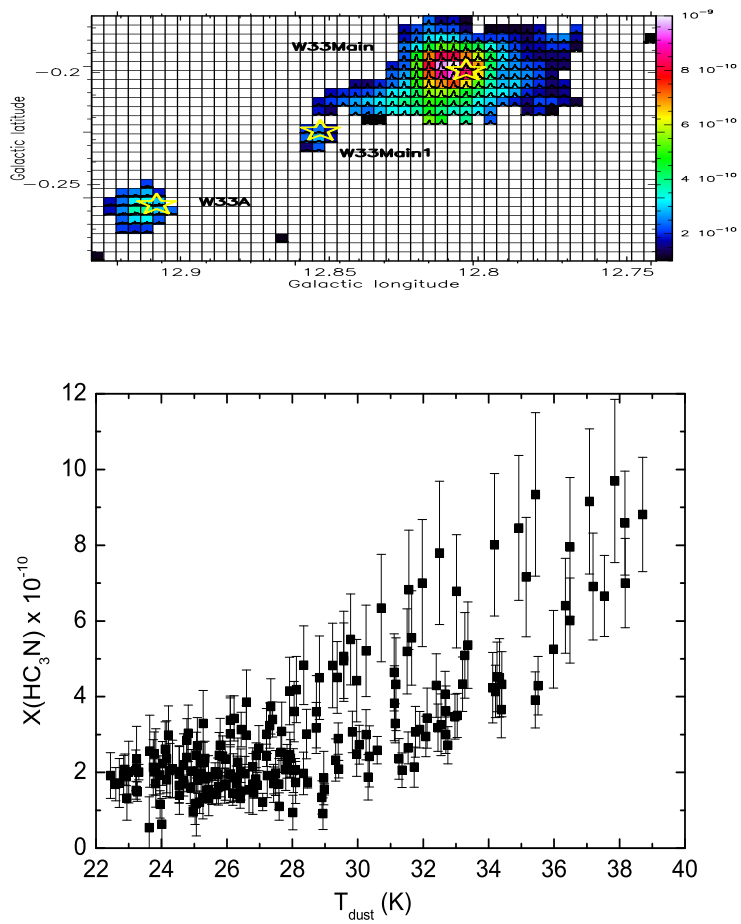


Figure 8. Top: The HCO^+ (1-0) spectra superimposed on the calculated HC_3N abundance map of G12.804-0.199. Bottom: Abundance of HC_3N plotted as a function of the dust temperature in each pixel of G12.804-0.199.

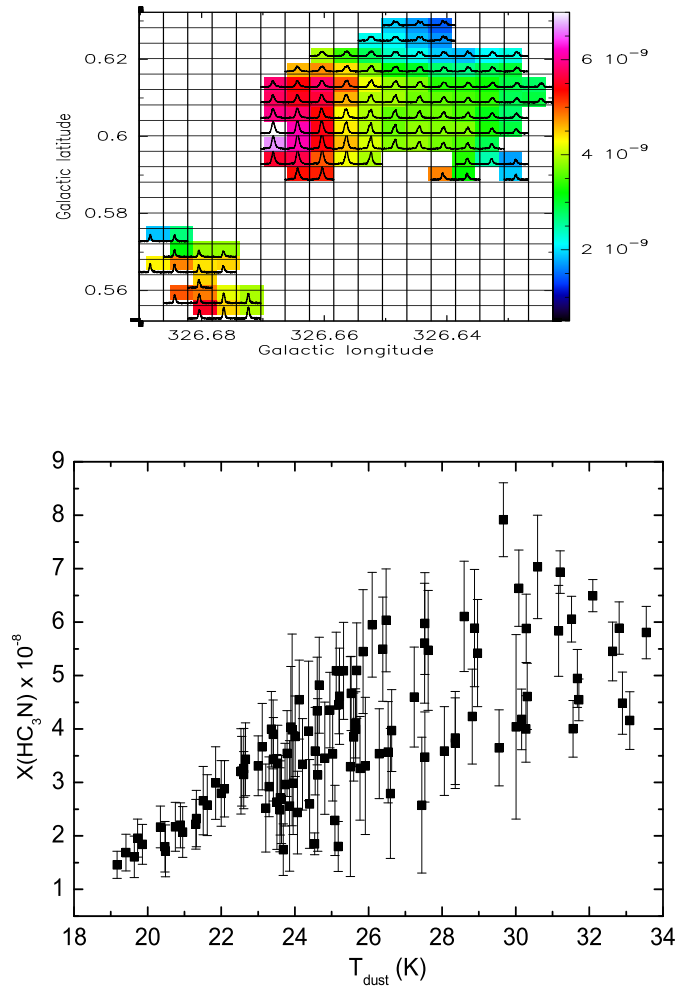


Figure 9. Top: The HCO⁺ (1-0) spectra superimposed on the calculated HC₃N abundance map of G326.641+0.612. Bottom: Abundance of HC₃N plotted as a function of the dust temperature in each pixel of G326.641+0.612.

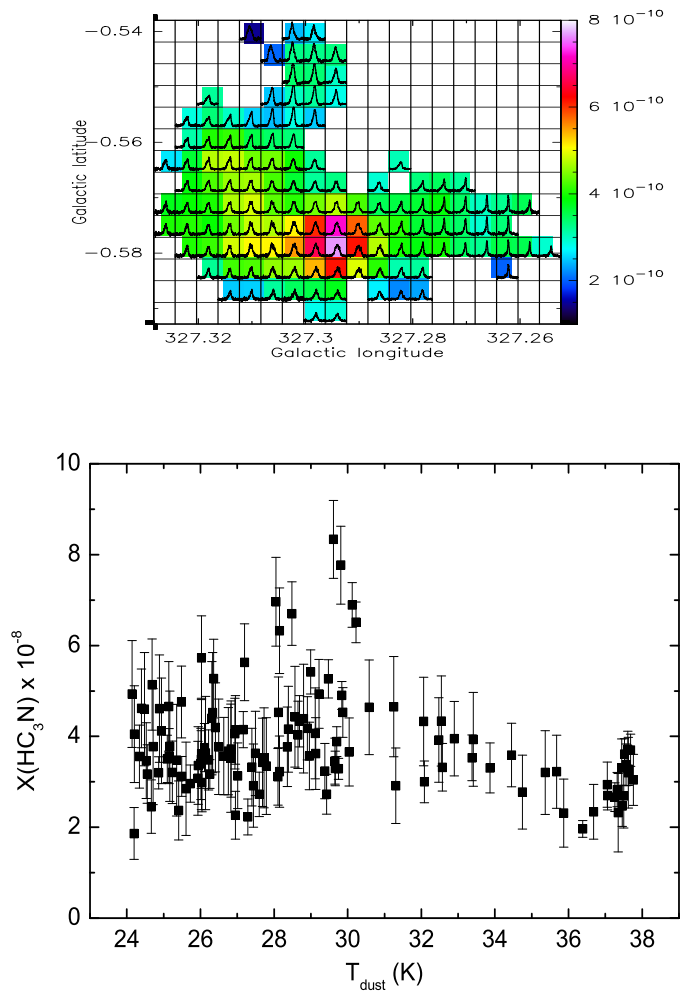


Figure 10. Top: The HCO^+ (1-0) spectra superimposed on the calculated HC_3N abundance map of G327.293-0.579. Bottom: Abundance of HC_3N plotted as a function of the dust temperature in each pixel of G327.293-0.579.

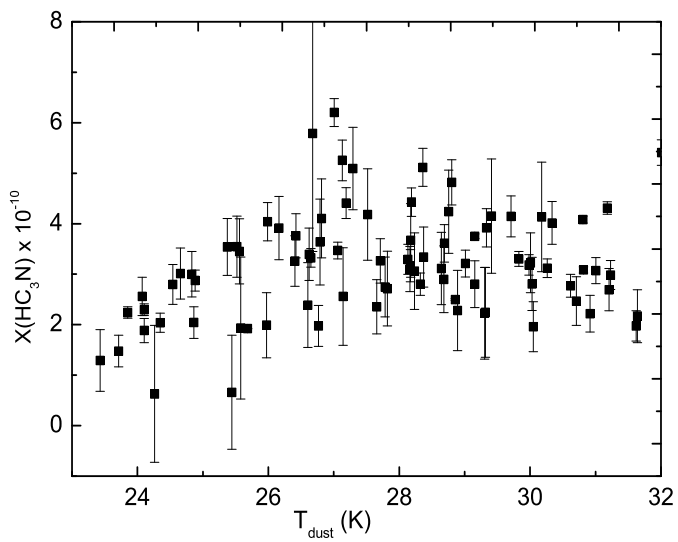
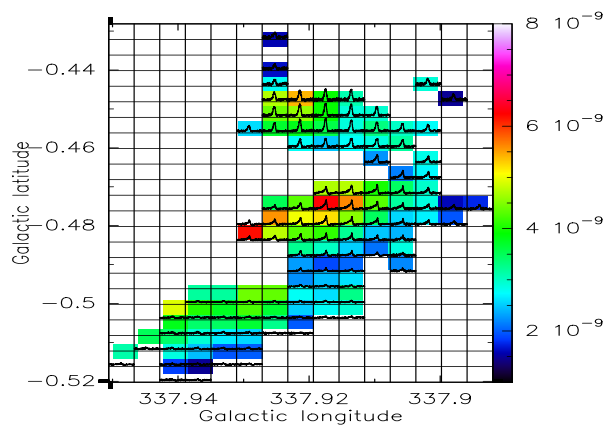


Figure 11. Top: The HCO^+ (1-0) spectra superimposed on the calculated HC_3N abundance map of G337.916-0.477. Bottom: Abundance of HC_3N plotted as a function of the dust temperature in each pixel of G337.916-0.477.

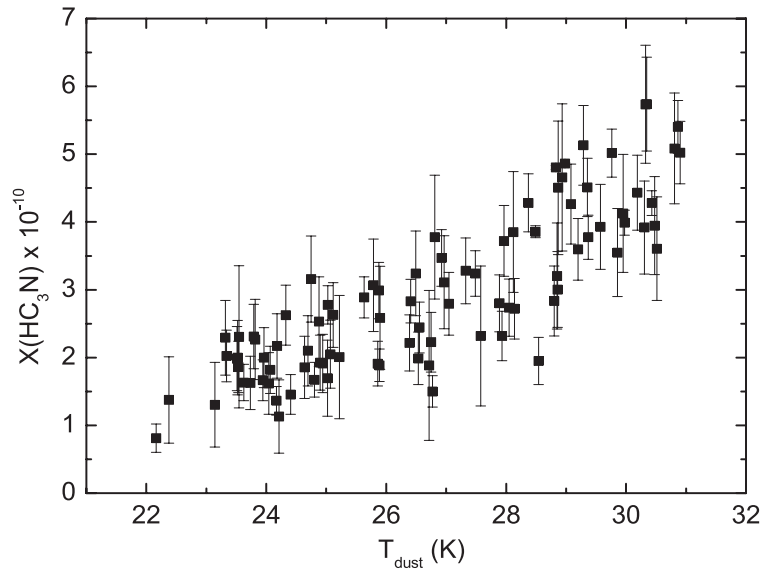
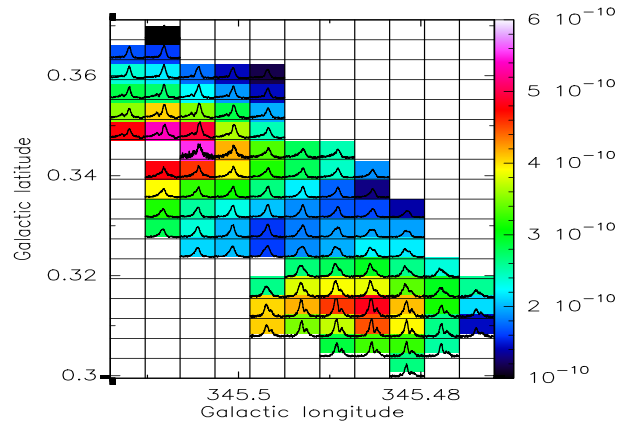


Figure 12. Top: The HCO^+ (1-0) spectra superimposed on the calculated HC_3N abundance map of G345.448+0.314. Bottom: Abundance of HC_3N plotted as a function of the dust temperature in each pixel of G345.448+0.314.

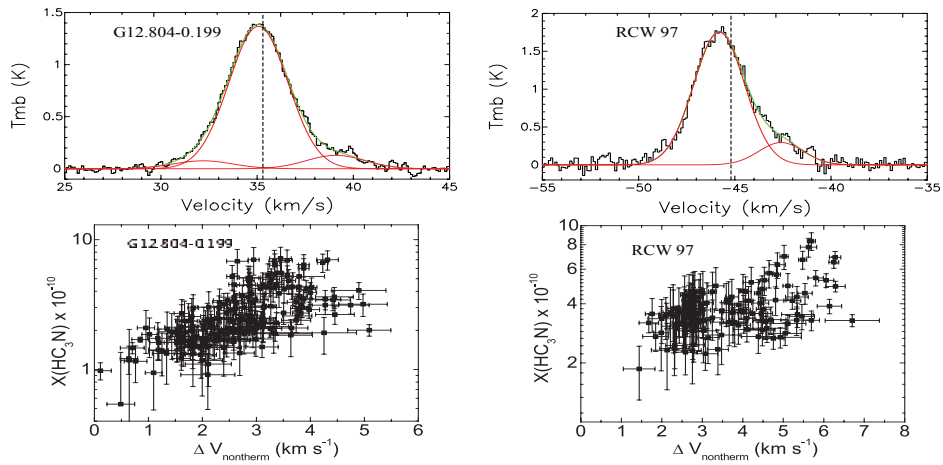


Figure 13. Top panels: The averaged spectra of HC_3N (10-9) in G12.804-0.199 and RCW 97 where its abundance is highest. Gaussian fits to individual components are plotted using solid red lines and the cumulative fits with solid green lines. Vertical dashed lines mark the systemic velocity of each source measured from the Gaussian fit to their N_2H^+ (1-0) lines. Bottom panels: The abundance of HC_3N plotted as a function of its nonthermal line width in G12.804-0.199 and RCW 97.

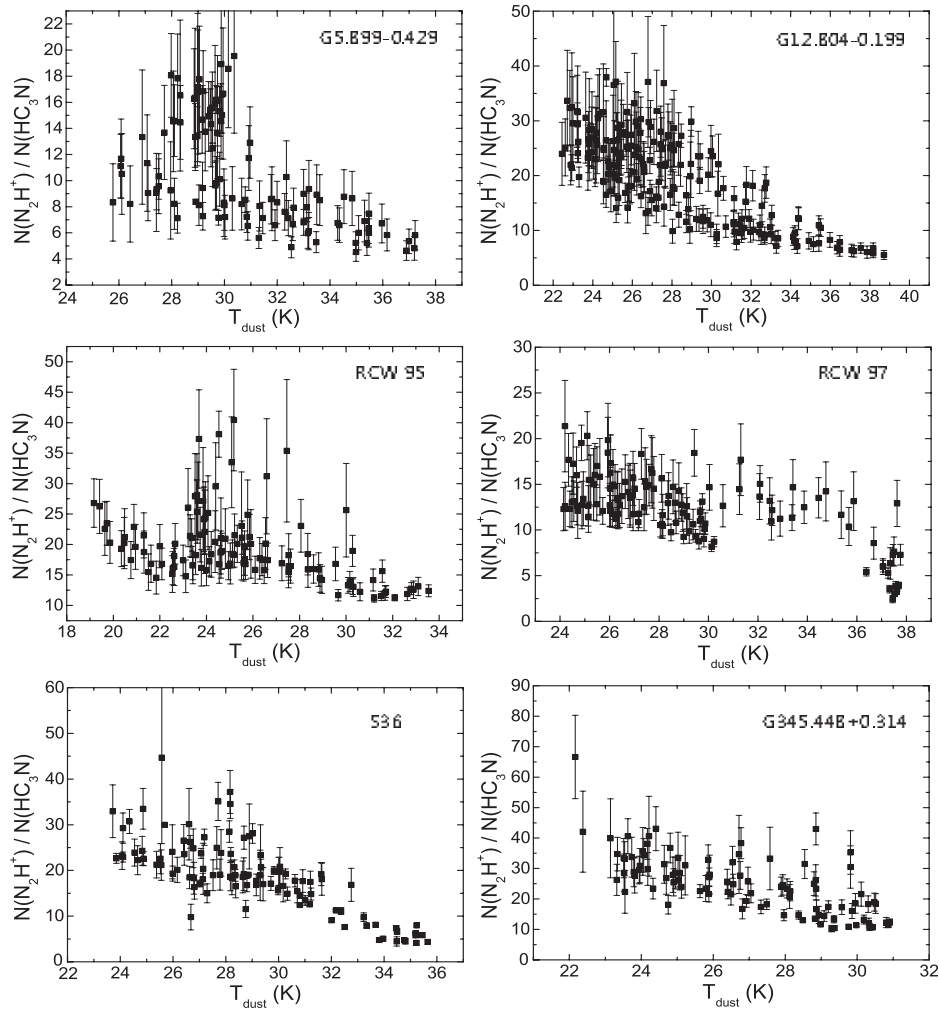


Figure 14. The relationship between $N(N_2H^+)/N(HC_3N)$ and T_{dust} in all of our sources. For RCW 95 and S36, the column densities of N_2H^+ are from YXW18. For other sources, we calculated their column densities of N_2H^+ in the same way.